ACS APPLIED MATERIALS & INTERFACES

Research Article

www.acsami.org

Synthesis and Characterization of One-Dimensional Ag-Doped ZnO/Ga-Doped ZnO Coaxial Nanostructure Diodes

Hsien-Ming Chiu,[†] Yu-Tsui Chang,[‡] Wen-Wei Wu,[‡] and Jenn-Ming Wu*[,†]

[†]Department of Materials Science and Engineering, National Tsing Hua University, Hsinchu 30013, Taiwan (ROC)

[‡]Department of Materials Science and Engineering, National Chiao Tung University, Hsinchu 30010, Taiwan (ROC)

ABSTRACT: In the pursuit of high injection current diode nanodevices, entire one-dimensional (1D) ZnO coaxial nanostructures with p−n homojunctions is one of the ideal structures. In this study, we synthesized entire 1D ZnO-based coaxial homojunction diodes with p-type Ag-doped ZnO (SZO) nanostructure shells covering n-type Ga-doped ZnO (GZO) nanopagoda (NPG) cores by a metal−organic chemical vapor deposition (MOCVD) technique. The entire 1D SZO−GZO and SZO−ZnO coaxial nanostructures exhibit better diode characteristics, such as lower threshold voltage, better rectification ratios, and better ideality factor *n*, than that reported for either 2D or 2D−1D p−n heterojunction and/or homojunction diodes. The binding energies of Ga and Ag were evaluated by low-temperature and temperature-dependent photoluminescence. In comparison, the SZO−GZO coaxial p−n nanostructures display better diode performance than the SZO−ZnO ones.

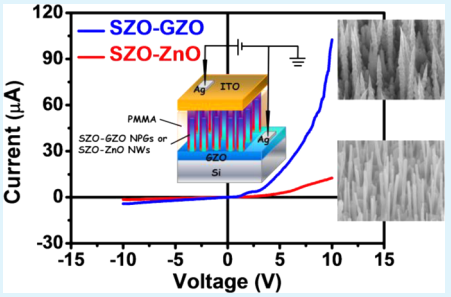

KEYWORDS: *zinc oxide, nanostructures, p−n homojunction, diode, MOCVD, binding energy*

1. INTRODUCTION

Zinc oxide, a II−VI n-type semiconductor with a direct energy gap of 3.37 eV and a large exciton binding energy of 60 meV,[1] is a good candidate material to substitute silicon for the pursuit of the next generation electronic and photonic devices. Many efforts had been devoted to develop ZnO nanostructures for various applications such as laser diodes,[1,2] light-emitting diodes,[3,4] solar cells,[5] field effect transistors,[6,7] field emitter,[8] photodetectors,[9,10] and photocatalysts.[9] Among them, diodes and light-emitting diodes attracted global interest recently due to the energy saving and environmental issues.

ZnO is an intrinsic n-type material due to its native defects like oxygen vacancies and zinc interstitials. The fabrication of reproducible p-type ZnO is relatively difficult. Hence, most of the ZnO-based diodes and light-emitting diodes used GaN,[4,11] polymer,[12,13] Si,[14] graphene,[15] $CuAlO_2$,[16] and CuAlCN[17] as p-type materials. However, as heterojunction devices, they exhibited lower efficiencies than homojunction devices due to the energy barriers formed at the junction interfaces, which decreased the carrier injection efficiency with a large band offset.[4]

Recently much progress has been made in ZnO-based p−n homojunction devices. Most of them are two-dimensional (2D), filmlike, ZnO-based p−n homojunctions. Although the carrier injection efficiency was improved by forming homojunctions instead of heterojunctions, the drawbacks include fair crystal qualities, nonsingle crystalline, and small junction areas. On the contrary, one-dimensional (1D) nanostructures such as wires, rods, tubes, rings, belts, needles, and pagodas are fascinating materials due to their unique properties like high aspect ratio and high surface area.[18] Diodes and light-emitting diode devices with high injection current and quantum effect light emission could be obtained using nanosized junctions formed by crossing p- and n-type nanowires.[11]

To obtain the aforementioned advantages and to pursue the next generation high injection current diode nanodevices, employment of entire 1D ZnO nanostructures with p−n homojunctions is one approach. It will maximize the junction areas and improve the crystal qualities.

Nowadays, only a few works about entire 1D ZnO-based p−n homojunction diodes or light-emitting diodes were reported. These works focused on using the group V^A elements, P and Sb,[19−22] as well as group I^A elements, K,[23] as the p-type dopants. In contrast, group I^B elements, which are quite different from group A elements as selective p-type dopants, have not been reported yet. A few reports predicted theoretically that Ag is a more efficient p-type acceptor than Cu and Au in ZnO due to its much shallower levels. The formation energy of Ag in favorable O-rich conditions (~0.85 eV) and the ionization energy of Ag (~0.4 eV) predicted by generalized gradient approximation with U values corrections (GGA+U) calculation are relatively lower than those for Cu and Au.[24−26]

In this study, we successfully synthesized 1D, p-type, Ag-doped ZnO nanowires (NWs) using the group I^B p-type dopants for the first time. We demonstrated entire 1D ZnO-based p−n homojunction diodes with p-type, Ag-doped, ZnO (SZO) nanostructure shells covering n-type, Ga-doped ZnO (GZO) nanopagoda (NPGs) cores by a metal−organic chemical vapor deposition (MOCVD) technique. The

Received: January 22, 2014
Accepted: March 12, 2014
Published: March 12, 2014

   dx.doi.org/10.1021/am500470y | *ACS Appl. Mater. Interfaces* 2014, 6, 5183−5191

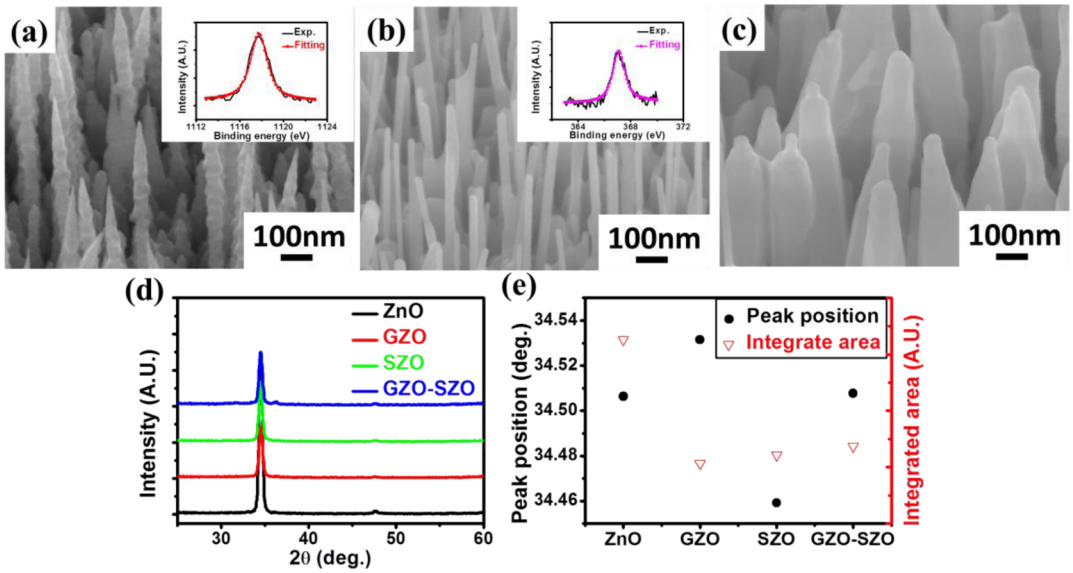

Figure 1. Typical SEM images of the (a) GZO NPGs (Ga/Zn precursor ratio =0.308); (b) SZO NWs (Ag/Zn precursor ratio = 0.360); and (c) SZO−GZO coaxial nanostructures. The insets in parts a and b are the experimental and fitting curves of the Ga $2p_{3/2}$ and Ag $3d_{5/2}$ XPS signals, respectively. (d) GIXRD patterns carried out under a 0.5° grazing angle. (e) Position and integrated area of the ZnO (0002) peak for ZnO NWs, GZO NPGs, SZO NWs, and SZO−GZO coaxial nanostructures.

fabricated SZO NWs were characterized by low-temperature photoluminescence and electrical current−voltage (I−V) measurements, demonstrating that SZO possessed prominent p-type behavior. Finally, the influence of Ga content on the performances of p−n SZO−GZO coaxial nanostructure homojunction diodes was discussed.

2. EXPERIMENTAL SECTION

2.1. Deposition of the GZO Seed Layer. The GZO seed layer was deposited on Si (100) substrates by radio frequency (RF) magnetron sputtering at room temperature using a 1 % GZO target. The silicon substrates were cleaned by a method usually used in semiconductor technology before loading into the chamber. The sputtering power was kept at 45 W; working pressure 10 mTorr; sputtering gas 100 % Ar; and the deposition time 1 h. The as-deposited GZO seed layer was characterized by the Hall measurement. Its carrier concentration was 1.07×10^{20} 1/cm^3, mobility 65.22 cm^2/(V s), and resistivity 8.96×10^{-4} Ω cm. The electrical properties of the GZO seed layer are excellent to serve as back electrodes for further optoelectronic device measurements and applications.

2.2. Growth of SZO−GZO Coaxial Core−Shell Nanostructures. GZO nanostructure cores were fabricated on the predeposited GZO seed layer with a mask covered on the edge of the bottom electrode by MOCVD. Zinc acetylacetonate hydrate [$Zn(acac)_2 \cdot xH_2O$] (Aldrich, powder), oxygen gas, and gallium acetylacetonate [$Ga(acac)_3$] (Aldrich, 99.99 %) were used as the Zn, O, and Ga sources. Nitrogen was introduced as the precursor carrier gas. $Zn(acac)_2 \cdot xH_2O$ and $Ga(acac)_3$ powders were placed together in an outer glass vessel. The fabrication process was carried out in a horizontal quartz furnace at 750 °C; the outer precursor vessel was heated at 135 °C. The O_2 and N_2 flow rates were kept at 300 and 500 sccm, respectively; the working pressure was maintained at 3−4 Torr by a mechanical pump; and the reaction time was 30 min. For GZO nanostructures, the Ga/Zn precursor molar ratios were controlled to be 0.103, 0.308, 0.615, and 0.819. The fabricated GZO exhibits a pagoda shape. Pure ZnO NWs were also prepared by the same procedure without Ga doping.

The SZO nanostructure shells were grown onto the as-grown ZnO or GZO nanostructures by substituting silver pivalate [Ag(piv)] (Multivalent, 99.99 %) for $Ga(acac)_3$. The $Zn(acac)_2 \cdot xH_2O$ and Ag(piv) powders were placed separately in an outer glass vessel. The fabrication process was also carried out in a horizontal quartz furnace at 750 °C. The outer precursor vessel with $Zn(acac)_2 \cdot xH_2O$ and Ag(piv) was heated at 135 and 200 °C, respectively; the reaction time was 1 h. Other reaction parameters were the same as the fabrication of GZO nanostructures. For SZO nanostructures shells, the Ag/Zn precursor molar ratio was kept at 0.360. The obtained SZO has a wire shape.

2.3. Characterization of SZO−GZO Coaxial Core-Shell Nanostructures. The surface morphologies and crystal phases of the as-grown nanostructures were examined by field emission scanning electron microscope with an accelerating voltage of 15 kV (FESEM, JEOL JSM-6500) and by a grazing incident X-ray diffraction technique with Cu Kα radiation (GIXRD, PANalytical X'Pert Pro MRD), respectively. The chemical compositions and binding states of GZO NPGs and SZO NWs were investigated by X-ray photoelectron spectroscopy (XPS, PHI-1600). The crystal structures of SZO−GZO coaxial nanostructures were observed by a spherical-aberration corrected field emission atomic resolution analytical electron microscope at an accelerating voltage of 200 kV (Cs-corrected FE-STEM, JEOL JEM-ARM200F). Low-temperature photoluminescence (PL) measurements were carried out using the 325 nm line excitation from a He−Cd laser under 10 K with a cyclic liquid He cooling system (HORIBA iHR550). Temperature-dependent PL measurements were also carried out between temperatures from 10 to 300 K using the same instrument.

2.4. Electrical Properties of Two-Terminal SZO−GZO Coaxial Core−Shell Nanodevices. To determine the influences of the Ga content on the performances of the SZO−GZO coaxial p−n homojunction diodes, two-terminal nanodevices based on p−n homojunction diodes were fabricated by the following processes. Firstly, a poly(methyl methacrylate) (PMMA) film was spin-coated onto the as-grown SZO−ZnO or SZO−GZO coaxial nanostructures with a protecting film covered on the edge of the defined bottom electrode area, followed by a hard baking carried out at 70 °C for 30 min in an oven. Then, to remove the excess PMMA on top of the SZO−ZnO or SZO−GZO coaxial nanostructures, oxygen plasma treatment was employed by a plasma stripper system with an RF power of 25 W, O_2 flow rate of 30 sccm, and working pressure of 0.1 Torr. Next, a top conducting indium tin oxide (ITO) film was deposited by RF magnetron sputtering under room temperature using commercial 99.99 % ITO. After the ITO sputtering, the protecting film on the edge of the bottom electrode was stripped off for the next

Table 1. *I*–*V* Characteristics of SZO–ZnO and SZO–GZO with Different Ga/Zn Precursor Ratio Coaxial Nanostructures

Ga/Zn precursor ratios	Ga contents [%][a]	V_T [V][b]	forward bias current (10 V) [μA]	reverse bias current (−10 V) [μA]	rectification ratio	ideality factor	series resistance [kΩ]
0	0	3.22	12.6	1.44	8.8	5.9	47.7
0.103	2.9	1.46	37.6	2.88	13.1	3.8	18.6
0.308	4.9	1.28	102.5	4.19	24.5	2.9	10.2
0.615	6.6	1.15	23.6	6.05	3.9	9.3	32.3
0.819	8.0	2.08	10.6	2.46	4.3	7.9	60.4

[a]Quantification by X-ray photoelectron spectroscopy (XPS). [b]V_T: the threshold voltage is defined as the electric voltage producing forward bias current of 1 μA.

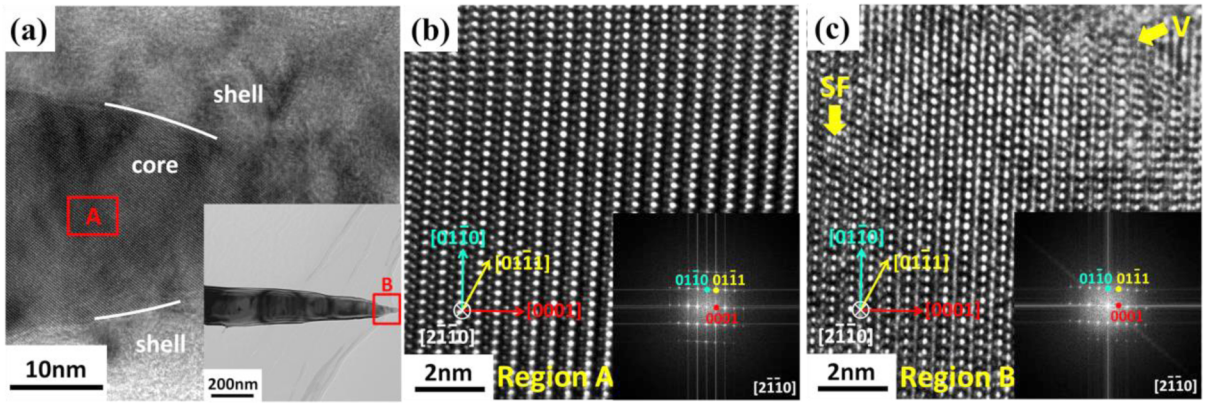

Figure 2. TEM images of a single SZO–GZO coaxial nanostructure: (a) high-magnification image; (inset) low-magnification image. HR-TEM images of (b) GZO core (region A in part a) and (c) SZO shell (region B in the inset of part a); (insets) their corresponding FFT diffraction patterns.

deposition of Ag electrode. Finally, patterned Ag electrode was RF magnetron sputtered with a hard mask using 99.99 % Ag target on the sample. *I*–*V* characteristics of the as-fabricated two-terminal nanodevices were measured by a semiconductor analyzer (Agilent B1500A) at room temperature.

3. RESULTS AND DISCUSSION

3.1. Characteristics of GZO NPGs, SZO NWs, and SZO–GZO Coaxial Nanostructures. *3.1.1. Morphology, Chemical Composition, and Crystal Structure.* Figure 1a shows the typical SEM image of the GZO NPGs cores (Ga/Zn precursor ratio = 0.308). The GZO NPGs cores are vertically-aligned with corrugated lateral surfaces similar to a pagoda shape. When the Ga/Zn precursor ratio was higher than 0.103, the shape of NPGs did not change significantly.[8] Pure ZnO nanostructures fabricated under the same process have a wire shape (ZnO NWs). The inset shows the Ga $2p_{3/2}$ core-level XPS signal obtained from the GZO NPGs shown in Figure 1a. The peak is located at 1117.7 eV. The determined Ga content by XPS ranges from 2.9 to 8.0% for the Ga/Zn precursor ratio changing from 0.103 to 0.819 (Table 1). Figure 1b shows the SEM image of the SZO nanostructures, exhibiting a wire-shape. The diameters and densities of the SZO NWs are similar to those of the GZO NPGs. The inset in Figure 1b shows the Ag $3d_{5/2}$ core-level XPS signal obtained for the SZO NWs. The peak located at 367.1 eV is without any component around 368.4 eV. This means that the Ag signal is due to Ag_{Zn} only and is without the presence of Ag metal or Ag_2O.[27] The Ag content was determined to be about 1.5%. The relatively low value of the Ag content as compared with the Ga content might be attributed to the larger ionic size mismatch: Ga^{3+} ions (0.47 Å), Zn^{2+} ions (0.60 Å), and Ag^{+} ions (1.00 Å).[28] The mismatches between ionic radii were about −21.6 and 66.7% for the substitution of Ga and Ag for Zn, respectively. Figure 1c shows the SEM image of the SZO–GZO coaxial core–shell nanostructures. Noticeably, the corrugated pagoda shape of the GZO NPG cores almost disappeared when they were covered by SZO shells. The SZO–GZO coaxial nanostructures lengthened and coarsened as compared with GZO NPGs, indicating that the SZO–GZO coaxial nanostructures grew not only along the fastest axial *c*-axis but also along the radial directions.

To characterize the top 1D nanostructure rather than the bottom seed layer and substrate, GIXRD was employed to reveal the crystal structures of the 1D nanostructure. Figure 1d shows the GIXRD patterns carried out under a 0.5° grazing angle for nanostructure samples. All GIXRD patterns show an intensive, sharp (0002) diffraction peak of ZnO at ca. 34.52° accompanying with two very weak diffractions, i.e. 36.32° ($10\bar{1}1$) and 47.52° ($10\bar{1}2$). It indicates that the ZnO NWs, GZO NPGs, SZO NWs, as well as SZO–GZO coaxial nanostructures are almost vertical to the substrates with only a slight tilt. The appearance of the (0002) preferred orientation of these nanostructures is partly due to the (0002) preferred orientation of the GZO seed layer and partly due to the fact that polar Zn^{2+}-terminated (0001) and O^{2-}-terminated ($000\bar{1}$) planes possess higher surface energies than other planes.[29,30] Therefore, the fastest growth direction occurs along the *c*-axis so that the (0002) preferred orientation is commonly found in wurtzite ZnO nanostructures. The peak intensity decreases noticeably with the Ga or Ag doping. The integrated intensities of the (0002) peak of the ZnO NWs, GZO NPGs, SZO NWs, and SZO–GZO coaxial nanostructures are plotted in Figure 1e, demonstrating that the integrated intensity decreases rapidly with the doping of either Ga or Ag. The full width at half maximum (FWHM) values are 0.45, 0.45, and 0.47° for ZnO

dx.doi.org/10.1021/am500470y | ACS Appl. Mater. Interfaces 2014, 6, 5183–5191

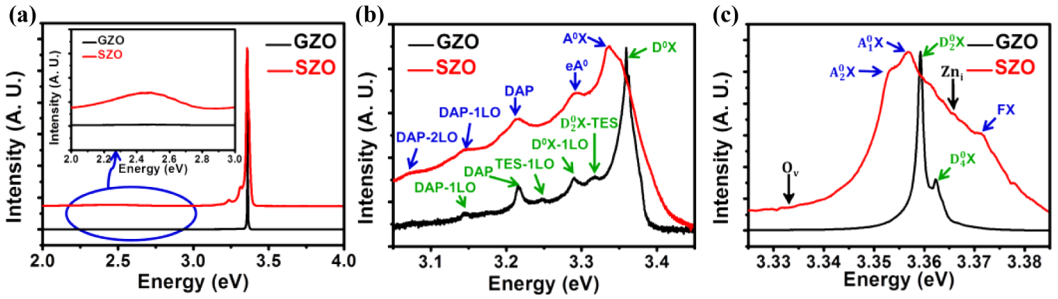

Figure 3. Low-temperature PL spectra of (a) the entire region, (inset) magnified plot of the DL region; (b) magnified plot of the NBE region; and (c) highly magnified plot of the NBE region of GZO NPGs (Ga/Zn precursor ratio = 0.308) and SZO NWs (Ag/Zn precursor ratio = 0.360) carried out at 10 K.

NWs, GZO NPGs, and SZO NWs, respectively, indicating that their crystal qualities are similar. Since the diameters and densities of the GZO NPGs and SZO NWs are not significantly different from those of the ZnO NWs, the decreased integrated intensities of the GZO and SZO NWs are attributed to the decreased axial growth rate caused by Ga or Ag doping.[8] The integrated intensity of the (0002) peak of the SZO NWs is slightly higher than that of the GZO NPGs because the SZO NWs possess a faster axial growth rate and thus higher volume than GZO NPGs. Moreover, the (0002) peak of the GZO NPGs shifts to higher angles, indicating that the decrease of lattice parameter c is due to the smaller Ga^{3+} ions (0.47 Å) substituting for larger Zn^{2+} ions (0.60 Å). In contrast, the shifting of the (0002) peak of the SZO NWs to lower angles is due to the larger Ag^{+} ion (1.00 Å) substituting for the Zn^{2+} ion. Similar phenomenon is also observed in SZO−GZO coaxial nanostructures.

Furthermore, to determine the change of the orientation of ZnO-based nanostructure samples obtained by gonio scan XRD analysis, the Lotgering factor (F) is calculated. The Lotgering factor (F) is defined as follows:[31,32]

$$F_{0002} = \frac{P_{0002} - P_0}{1 - P_0} \quad (1)$$

where, $P_{0002} = I_{0002}/\sum I_{hkl}$ and $P_0 = I^0_{0002}/\sum I^0_{hkl}$; with I_{0002} and I^0_{0002} being the intensities of (0002) peak for the textured and randomly (JCPDS No. 36-1451) oriented samples, respectively. The calculated F_{0002} are 0.97, 0.97, 0.97, and 0.96 for ZnO NWs, GZO NPGs, SZO NWs, and SZO−GZO coaxial nanostructures, accordingly. The (0002) preferred orientation was almost not changed for all the ZnO nanostructures.

Figure 2a displays a TEM image of a single SZO−GZO coaxial nanostructure shown in Figure 1c. The inset is a low-magnification image. The contour between the GZO core and the SZO shell is well-defined. Figure 2b shows the HR-TEM image taken from region A marked in Figure 2a, demonstrating the excellent crystal quality of the GZO core. The lattice spacing of the (0001) planes is measured as 0.523 nm. Crystal planes as well as directions could be deduced by fast Fourier transform (FFT) as a diffraction pattern with a $[2\bar{1}\bar{1}0]$ zone axis (inset).

Figure 2c also shows the HR-TEM image taken from region B marked in the inset of part a, demonstrating that the lattice of the SZO shell is slightly distorted. Defects like vacancy (V) and stacking faults (SF) are denoted by yellow arrows. These defects could be attributed to strains resulting from the much larger Ag^{+} ions substituting for Zn^{2+} ions. The lattice spacing of the (0001) planes is measured as 0.538 nm, which is slightly larger than that of the GZO core. The diffraction pattern shown in the inset has a $[2\bar{1}\bar{1}0]$ zone axis as deduced by FFT, demonstrating that the SZO shell is also single crystalline. The crystallographic orientation relationships between the GZO core and the SZO shell are identified as below:

$$[2\bar{1}\bar{1}0]_{GZO,core}//[2\bar{1}\bar{1}0]_{SZO,shell}$$

$$(0002)_{GZO,core}//(0002)_{SZO,shell}$$

This demonstrates the epitaxial nature of the SZO−GZO coaxial homojunction.

3.1.2. Photoluminescence, Binding Energy, and Activation Energy. Low-temperature (10 K) PL spectra shown in Figure 3 could provide useful insights into the energy levels of either donors in the GZO NPGs or acceptors in the SZO NWs. Figure 3a shows the low temperature (10 K) PL spectra of the GZO NPGs (Ga/Zn precursor ratio = 0.308) and the SZO NWs. Both nanostructures show only a prominent near-band-edge (NBE) peak near 3.360 eV, which is attributed to the emission by free excitons, polaritons, and bound excitons, revealing that these two nanostructures possess excellent crystal qualities. Broad deep-level emission (DL) around 2.5 eV which is usually contributed by defects like oxygen vacancies and zinc interstitials is not observed. If the DL region is enlarged (inset), a very weak DL peak is found in SZO NWs while none is observed in GZO NPGs. This is consistent to the TEM observations shown in Figure 2.

Figure 3b is a magnified plot of the NBE region with a log scale intensity, demonstrating that GZO NPGs possess dominant donor bound excitons (D^0 X) at 3.360 eV, while SZO NWs possess dominant acceptor bound excitons (A^0 X) at 3.353 eV. This suggests that GZO NPGs and SZO NWs are n- and p-type, respectively. In GZO NPGs, other peaks could be indexed as D^0_2 X-TES (3.318 eV) in the two-electron satellite (TES) transition region and as D^0 X-1LO (3.291 eV), TES-1LO (3.248 eV), DAP (3.217 eV), and DAP-1LO (3.146 eV) in the donor−acceptor pair (DAP) transition and longitudinal optical (LO) phonon replicas region. If we examine the donor bound excitons (D^0 X) peak further, it splits into two component peaks: D^0_2 X and D^0_4 X at 3.360 and 3.363 eV, respectively, as shown in Figure 3c.[33] The D^0_2 X line at 3.360 eV is very close to the I_8 line at 3.359 eV, which is associated with the recombination of exciton bound to neutral Ga-donor observed by Meyer et al.[34] The TES transitions involve irradiative recombination of an exciton bound to a neutral donor, leaving the donor in the excited state. The energy difference between the ground-state neutral donor bound excitons and their excited states (TES) can be used to

dx.doi.org/10.1021/am500470y | ACS Appl. Mater. Interfaces 2014, 6, 5183−5191

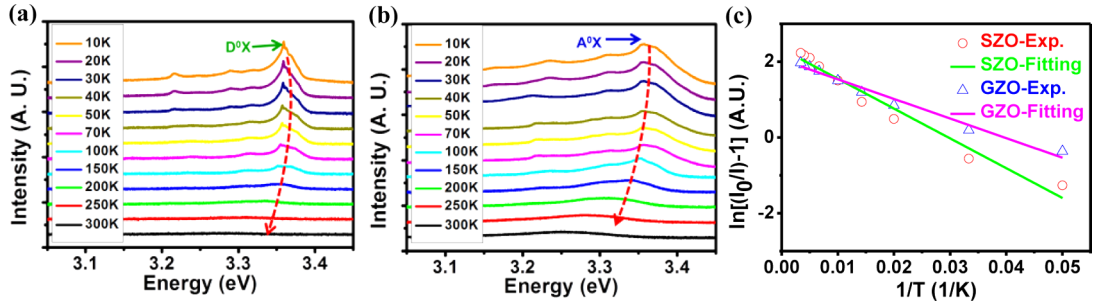

Figure 4. Temperature-dependent PL spectra of (a) GZO NPGs (Ga/Zn precursor ratio = 0.308). (b) SZO NWs (Ag/Zn precursor ratio = 0.360). (c) Experimental data and the fitted Arrhenius plots of the PL intensities of D^0 X and A^0 X as a function of the reciprocal temperature for the GZO NPGs and SZO NWs, respectively.

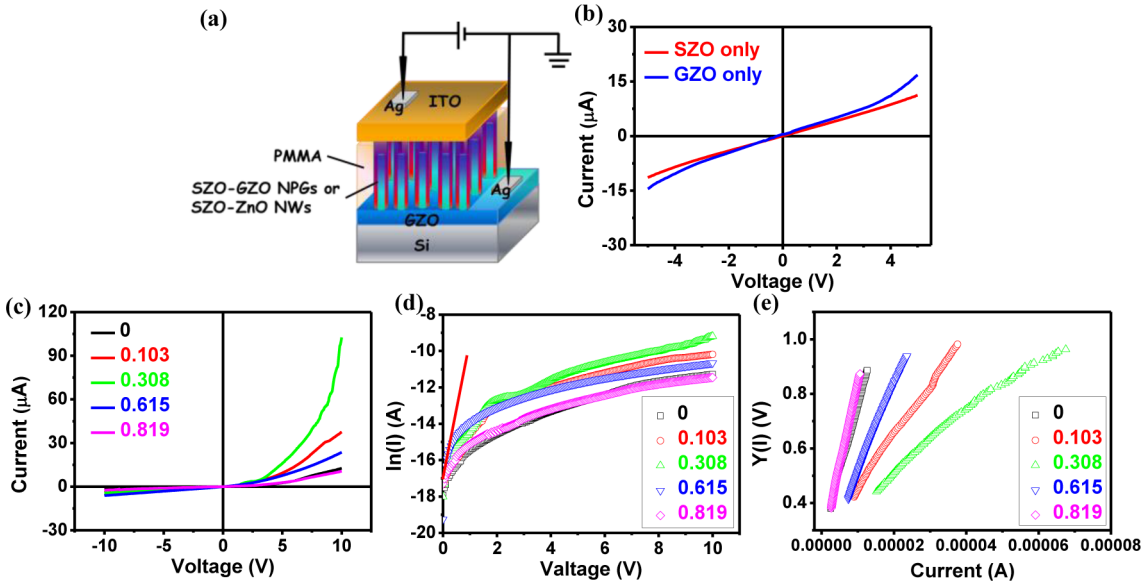

Figure 5. (a) Schematic of the SZO−ZnO and SZO−GZO coaxial nanostructures p−n homojunction diodes. (b) *I*−*V* characteristic of the n-type GZO NPGs (Ga/Zn precursor ratio = 0.308) and p-type SZO NWs (Ag/Zn precursor ratio = 0.360). (c) *I*−*V*, (d) ln(*I*)−*V*, and (e) *Y*(*I*)−*I* characteristics of the SZO−ZnO and SZO−GZO coaxial nanostructures with different Ga/Zn precursor ratios. The straight line in part d shows the region in which the ideality factor *n* values are calculated.

determine the donor binding energies (the donor excitation energy from the ground state to the first excited state equals to 3/4 of the donor binding energy, E_D).[33] Herein, the Ga binding energy in GZO NPGs is calculated as 56 meV using the ground stare D_2^0 X line at 3.360 eV and the first excited state D_2^0 X-TES line at 3.318 eV. This value is comparable to the 54.6 meV reported by Meyer et al.[34] and 60 meV reported by Zhu et al.[35]

On the other hand, we can also identify several other peaks in the SZO NWs as free electron-to-acceptor (eA^0) (3.310 eV) in the TES transitions region; and as DAP (3.217 eV), DAP-1LO (3.146 eV), and DAP-2LO (3.093 eV) in the DAP transitions and LO-phonon replicas region. Similarly, if we further examine the acceptor bound excitons (A^0 X), it is found to split into at least three component peaks as A_2^0 X, A_1^0 X, and free excitons (FX) emission at 3.353, 3.357, and 3.372 eV, respectively, as shown in Figure 3c.[33,36] Defects like oxygen vacancies (O_v) and zinc interstitials (Zn_i) usually appeared at about 3.333 and 3.366 eV, respectively.[37,38] From Figure 3c, no obvious peaks of oxygen vacancies (O_v) and zinc interstitials (Zn_i) could be found. When the temperature was raised (Figure 4), the PL emission intensity exhibited remarkable decrease. It is more difficult to find these defects in the temperature-dependent PL spectra. Therefore, the concentrations of oxygen vacancies (O_v) and zinc interstitials (Zn_i) are very low in these nanostructures.

To estimate the acceptor binding energies (E_A) of the Ag dopant, the eA^0 transition at 3.310 eV is useful. The E_A is evaluated by eq 2:[36]

$$E_A = E_g - E_{eA^0} + \frac{1}{2}k_BT \tag{2}$$

where, E_g is the band gap energy (3.437 eV at 10 K); k_B is the Boltzmann constant. The binding energy of Ag is calculated as 127 meV for the SZO nanostructure. This value is lower than the theoretically calculated results 400 meV[24,25] but is comparable with the reported data which varied from 117 to 158 meV.[39,40]

Figure 4a and b shows the temperature dependence of the PL spectra of GZO NPGs and SZO NWs, respectively, with temperatures ranging from 10 to 300 K. The remarkable decreasing of the D^0 X or A^0 X emission intensities near 3.360 eV and their concomitant shifting to lower energy (depicted by red dash arrows) with increasing temperature are due to the thermal dissociation of D^0 X and A^0 X to FX.

Figure 4c reveals the Arrhenius plots of the intensities of the D^0 X and A^0 X emissions as a function of reciprocal

dx.doi.org/10.1021/am500470y | ACS Appl. Mater. Interfaces 2014, 6, 5183−5191

temperature for the GZO NPGs and SZO NWs, respectively. The temperature-dependent activated behaviors of D^0 X and A^0 X emission are described as follows:[36]

$$I = I_0 / \left[1 + a\exp\left(\frac{-E_a}{k_B T} \right) \right] \quad (3)$$

where, I_0 is the intensity at zero temperature, which is approximately the same as that at T = 10 K; a is a proportional constant; E_a is the activation energy; and k_B is the Boltzmann constant. Equation 3 can be rearranged as below:

$$\ln\left[\left(\frac{I_0}{I} \right) - 1 \right] = a - \frac{E_a}{k_B T} \quad (4)$$

Either donor or acceptor activation energies can be obtained from the line slopes shown in Figure 4c. The Ga and Ag activation energies are estimated to be about 18.41 and 11.28 meV, respectively. Furthermore, the Haynes factor (β) is defined as follows:[41,42]

$$\beta = E_a / E_B \quad (5)$$

where, E_a is the activation energy and E_B is the binding energy. Taken from the values obtained above, we can deduce the β for Ga donors to be 0.33, using E_a = 18.41 meV and E_D = 56 meV, and deduce the β for Ag acceptors to be 0.09, taking E_a = 11.28 meV and E_A = 127 meV. These β values are very close to the value 0.3 for neutral donors (D^0 X) and 0.1−0.15 for neutral acceptors (A^0 X) in the ZnO system.[43]

3.2. Diode Performance of SZO−ZnO and SZO−GZO Coaxial Nanostructures. *3.2.1. I−V Characteristics.* To investigate the influences of the Ga content on the p−n characteristics of SZO−GZO coaxial nanostructures, two-terminal nanodevices based on p−n homojunction diodes were fabricated. The schematic diagram of the SZO−ZnO and SZO−GZO coaxial nanostructures is illustrated in Figure 5a. To make it easier to read, only one island of Ag electrode was drawn in Figure 5a. The linear ohmic I−V characteristics of the n-type GZO NPGs (Ga/Zn precursor ratio = 0.308) and the p-type SZO NWs are shown in Figure 5b. Both samples possess the same measuring arrangement as SZO−GZO coaxial nanostructures.

Figure 5c shows the I−V characteristic of the SZO−ZnO and SZO−GZO (with various Ga content in the GZO cores) coaxial nanostructures, exhibiting apparent nonlinear rectifying I−V behavior. The forward bias current increases dramatically with increasing Ga content and reach a maximum value at Ga/Zn precursor ratio = 0.308. Increasing Ga content raises the electron concentration in the n-region and enhances the electrical conductivity (σ_s) in SZO−GZO coaxial nanostructures. Higher forward bias current is obtained in SZO−GZO than in SZO−ZnO coaxial nanostructures. The forward bias current decreases when the Ga/Zn precursor ratio is higher than 0.308. It is partly due to the Burstein−Moss effect occurring in the high electron carrier concentration regime and partly due to the formation of complex defects (trap centers) at high Ga content. The threshold voltage (V_T), defined as the electric voltage producing a forward bias current of 1 μA, is also found to decrease significantly when increasing Ga is doped into ZnO. The V_T is about 1.28 and 3.22 V for SZO−GZO (Ga/Zn precursor ratio = 0.308) and SZO−ZnO coaxial nanostructures, respectively. Theoretically, the built-in potential would be increased by the increase of the donor concentration; nevertheless, we observed that the V_T decreased with the Ga content. It might be attributed to the band gap narrowing effect. The band of the impurity state widens, overlaps, and moves up toward the bottom of the conduction band. As the band gap narrows, the built-in potential decreases, resulting in smaller V_T. The decreased V_T with donor concentration was also found for GZO ultraviolet photodetectors and field emitters in our previous works,[8,9] and in diodes reported by Kim et al. and Ahn et al.[44,45] In heavily Ga doped SZO−GZO coaxial nanostructures such as the one with Ga/Zn precursor ratio = 0.819, the V_T was observed to increase again; this can be attributed to the Burstein−Moss effect. Zener breakdown occurring in heavily doped p−n junctions through a tunneling mechanism or Avalanche breakdown occurring in sufficient electrons or holes through a colliding mechanism is not observed when the applied reverse bias voltage is −10 V. The rectification ratio (RR) exhibited the same trend as the forward bias currents with a maximum RR of 24.5 (Ga/Zn precursor ratio = 0.308), which was approximately 2.8 times higher than that of the SZO−ZnO (RR = 8.8). Typical characteristics of SZO−GZO and SZO−ZnO coaxial nanostructures are summarized in Table 1.

3.2.2. Ideality Factor (n). Figure 5d shows the semi-log plot of I−V curves measured for SZO−ZnO and SZO−GZO coaxial nanostructures. Short linear regions are observed in the low voltage range. At high applied voltages, the devices deviate from the diodelike behavior. The diode I−V relationship can be written as follows:

$$I = I_s \left[\exp\left(\frac{eV}{nk_B T} \right) - 1 \right] \quad (6)$$

where, I_s is the reverse saturation current; n is the ideality factor; e is the elementary charge; k_B is the Boltzmann constant; and the (−1) term is negligible when V > 0.1 V. Equation 6 can be rearranged as below:

$$\ln I = \ln I_s + \frac{eV}{nk_B T} \quad (7)$$

By fitting the slope of the linear region at the low voltage range, the ideality factor n can be estimated as 5.9 and 2.9 for SZO−ZnO and SZO−GZO (Ga/Zn precursor ratio = 0.308) coaxial nanostructures, respectively (Table 1). High ideality factor (n > 2) in wide band gap semiconductor materials such as ZnO and GaN were usually reported. This high ideality factor suggests that the I−V characteristic is not limited by thermionic emission of the conventional p−n junction. It may also be attributed to several effects: (i) interface states at a thin oxide between the metal and the semiconductor; (ii) tunneling currents in highly doped semiconductors (also considered as deep-level-assisted tunneling); (iii) image force lowing of the Schottky barrier in the electric field at the interface; and (iv) generation/recombination currents within the space-charge region (also considered as space-charge-limited conduction (SCLC)).[46,47]

Factor iii can be ruled out due to the reasons that SZO−ZnO and SZO−GZO coaxial nanostructures are not Schottky diodes and the device has Ohmic contacts as demonstrated in Figure 5b. These secondary mechanisms cause the inhomogeneities at the interface within the device. Charge traps (or complex defects) may lead to a lateral inhomogeneous distribution of barrier heights, which then results in larger ideality factors and the charge transport across the interface is no longer due to

Table 2. Reported Performances of ZnO-Based p−n Heterojunction/Homojunction Diodes

p−n structures	V_T [V]	forward bias current [μA]	reverse bias current [μA]	rectification ratio	ideality factor	ref
2D polymer−ZnO film	3.45	30 (5 V)	70 (−5 V)	0.4 (±5 V)	2.93	13
2D polymer−ZnO film		0.12 (10 V)	0.03 (−10 V)	4 (±10 V)	8.74	54
2D SZO−ZnO film	7	70 (20 V)	40 (−20 V)	1.75 (±20 V)		55
2D SZO−GZO film	3	0.06 (5 V)	0.01 (−5 V)	6 (±5 V)		56
1D SZO nanowires−2D GZO film	3.8	300 (10 V)	300 (−10 V)	1 (±10 V)	1−7	57
2D MgGaN film−1D CuZO nanorods	2	20 (2 V)	28 (−2 V)	0.7 (±2 V)		58
1D SbZO−ZnO nanorods	3.3	160 (5 V)		105 (±5 V)	2.8 (<1 V) 18 (>1 V)	19
1D PZO−ZnO nanorods	0.8	5 (3 V)	1 (−3 V)	5 (±3 V)	3.8−17.5	20
1D PZO−ZnO single nanowire	1.37	0.5 (3 V)	2×10^{-4} (−3 V)	2500 (±3 V)	2.28	22
1D SZO−ZnO nanowires	3.22	12.6 (10 V)	1.44 (−10 V)	8.8 (±10 V)	5.9	this work
1D SZO−GZO nanopagodas	1.28	102.5 (10 V)	4.19 (−10 V)	24.5 (±10 V)	2.9	this work

thermionic emission only. The inhomogeneities may play an important role and have to be considered in the evaluation of experimental $I-V$ characteristics. The high ideality factors can be attributed to the presence of a wide distribution of low-barrier-height patches caused by laterally barrier inhomogeneity.[48] Comparing the ideality factors of the SZO−ZnO and SZO−GZO coaxial nanostructures with reported results, which were summarized in Table 2, our coaxial nanostructures exhibited relatively small ideality factors than those reported for heterojuction nanostructures.

3.2.3. Series Resistance (R_s). Series resistance (R_s) is also one of the key parameters that determine the electrical properties of the diode system. An alternate approach developed by Cheung et al.[49] is applied to calculate the R_s of diode in the downward curvature (nonlinear region) of the forward bias $I-V$ characteristics. In this approach, eq 8 shows the relation between I and R_s:[50,51]

$$I = I_s\left[\exp\left(\frac{e(V - IR_s)}{nk_BT}\right)\right] \tag{8}$$

where, the IR_s is the voltage drop across the series resistance of diode. Equation 8 can be reorganized as follows:

$$Y(I) = \frac{dV}{d\ln(I)} = IR_s + \frac{nk_BT}{e} \tag{9}$$

Figure 5e shows the variation of the $Y(I)$ function with I. There is a linear relation between I and the $Y(I)$ function. By calculating the slopes, the R_s values are evaluated and listed in Table 1. The result shows that series resistance R_s exhibits the inverse trend with the Ga/Zn precursor ratio as the forward bias current. The variation of series resistance R_s and forward bias current are compatible with each other and can be explained by the variation of conductivity with the Ga/Zn precursor ratio, which was discussed above.

The $I-V$ characteristics of the SZO−ZnO and SZO−GZO coaxial nanostructures are summarized in Table 2. The much low reverse bias current accompanying with the much high RR reported by Li et al.[22] was due to the device to be a single 1D PZO−ZnO nanowire. In contrast, the $I-V$ characteristics of the 1D SZO−ZnO and SZO−GZO coaxial nanostructures in this work were contributed by all coaxial nanostructures between top and bottom electrodes. Due to variations existing among coaxial nanostructures, the RR values are usually lower than that obtained for a single nanowire. These two coaxial nanostructures performed better diode characteristics, such as lower V_T, better RR, and better ideality factor n, than that reported for 2D and 2D−1D nanostructures, either p−n heterojunctions or homojunctions. This is partly due to the presence of homojunctions instead of heterojunctions and partly due to the increased area of nanosized junctions as well as the better crystal qualities of both the p and n 1D nanostructure.

In comparing these two coaxial nanostructures, the SZO−GZO possess smaller V_T (1.28 relative to 3.22 V), larger forward bias currents (102.5 respect to 12.6 μA), better RR (24.5 relative to 8.8), better ideality factor n (2.9 respect to 5.9), and smaller series resistance R_s (10.2 relative to 47.7 kΩ) than the SZO−ZnO coaxial nanostructures. It could be attributed to the much shallower levels of the Ga donor (56 meV) and the Ag acceptor (127 meV) than those of the intrinsic defects: 0.08−1.03 eV for zinc interstitials (Zn_i), 0.25−3 eV for oxygen vacancies (V_o), 0.26−0.35 eV for zinc vacancies (V_{Zn}), and 0.38−2.67 eV for oxygen interstitials (O_i).[52,53] The schematic energy levels are shown in Figure 6.

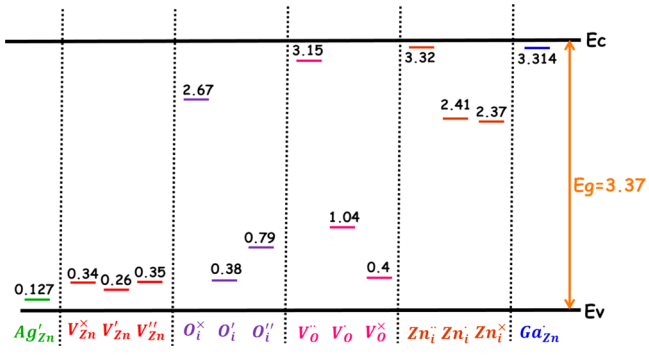

Figure 6. Schematic energy band diagram for ZnO-based nanostructures. All the energy levels are referred to as the valence band (E_V), and the unit of energy levels is electronvolts.

4. CONCLUSIONS

Entire 1D ZnO-based coaxial p−n homojunction diodes were fabricated by MOCVD. The n-type GZO NPGs cores were grown on GZO seed layers first, then the p-type SZO shells were deposited sequentially on the GZO NPGs. Entire 1D SZO−GZO and the SZO−ZnO coaxial nanostructures exhibit better diode characteristics, such as lower V_T, better RR, and

better ideality factor n, than that reported for 2D and 2D−1D p−n nanostructures, either heterojunctions or homojunctions. It is partly due to the presence of homojunctions instead of heterojunctions and partly due to the increased area of nanosized junctions and the better crystal qualities of both the p and the n 1D nanostructure. The binding energies of Ga and Ag were determined to be about 56 and 127 meV, respectively, by low-temperature and temperature-dependent photoluminescence. The SZO−GZO coaxial p−n nanostructures show better diode properties than those of SZO−ZnO.

AUTHOR INFORMATION

Corresponding Author

*E-mail: wu408410@yahoo.com.tw.

Notes

The authors declare no competing financial interest.

ACKNOWLEDGMENTS

The authors gratefully acknowledge the National Science Council of the Republic of China for the financial support under Contract No. NSC 99-2221-E-007-035-MY3. The authors also greatly appreciate the National Nano Device Laboratories for technical supports and the use of facility at CNMM of the National Tsing Hua University which is partly supported by the Ministry of Education, Republic of China (Taiwan).

REFERENCES

(1) Huang, M. H.; Mao, S.; Feick, H.; Yan, H. Q.; Wu, Y. Y.; Kind, H.; Weber, E.; Russo, R.; Yang, P. D. Room-Temperature Ultraviolet Nanowire Nanolasers. *Science* **2001**, *292*, 1897−1899.

(2) Kwok, W. M.; Djurisic, A. B.; Leung, Y. H.; Chan, W. K.; Phillips, D. L. Time-resolved Photoluminescence Study of the Stimulated Emission in ZnO Nanoneedles. *Appl. Phys. Lett.* **2005**, *87*, 093108.

(3) Willander, M.; Nur, O.; Bano, N.; Sultana, K. Zinc Oxide Nanorod-based Heterostructures on Solid and Soft Substrates for White-Light-Emitting Diode Applications. *New J. Phys.* **2009**, *11*, 125020.

(4) Park, W. I.; Yi, G. C. Electroluminescence in n-ZnO Nanorod Arrays Vertically Grown on p-GaN. *Adv. Mater.* **2004**, *16*, 87−90.

(5) Martinson, A. B. F.; Elam, J. W.; Hupp, J. T.; Pellin, M. J. ZnO Nanotube Based Dye-Sensitized Solar Cells. *Nano Lett.* **2007**, *7*, 2183−2187.

(6) Arnold, M. S.; Avouris, P.; Pan, Z. W.; Wang, Z. L. Field-effect Transistors Based on Single Semiconducting Oxide Nanobelts. *J. Phys. Chem. B* **2003**, *107*, 659−663.

(7) Yuan, G. D.; Zhang, W. J.; Jie, J. S.; Fan, X.; Tang, J. X.; Shafiq, I.; Ye, Z. Z.; Lee, C. S.; Lee, S. T. Tunable n-Type Conductivity and Transport Properties of Ga-doped ZnO Nanowire Arrays. *Adv. Mater.* **2008**, *20*, 168−173.

(8) Chiu, H.-M.; Tsai, H.-J.; Hsu, W.-K.; Wu, J.-M. Experimental and Computational Insights in the Growth of Gallium-doped Zinc Oxide Nanostructures with Superior Field Emission Properties. *Crystengcomm* **2013**, *15*, 5764−5775.

(9) Chiu, H.-M.; Wu, J.-M. Opto-electrical Properties and Chemisorption Reactivity of Ga-doped ZnO Nanopagodas. *J. Mater. Chem. A* **2013**, *1*, 5524−5534.

(10) Weng, W. Y.; Chang, S. J.; Hsu, C. L.; Hsueh, T. J.; Chang, S. P. A Lateral ZnO Nanowire Photodetector Prepared on Glass Substrate. *J. Electrochem. Soc.* **2010**, *157*, K30−K33.

(11) Jeong, M.-C.; Oh, B.-Y.; Ham, M.-H.; Lee, S.-W.; Myoung, J.-M. ZnO-Nanowire-Inserted GaN/ZnO Heterojunction Light-Emitting Diodes. *Small* **2007**, *3*, 568−572.

(12) Wadeasa, A.; Nur, O.; Willander, M. The Effect of The Interlayer Design on the Electroluminescence and Electrical Properties of n-ZnO Nanorod/p-Type Blended Polymer Hybrid Light Emitting Diodes. *Nanotechnology* **2009**, *20*, 065710.

(13) Zaman, S.; Zainelabdin, A.; Amin, G.; Nur, O.; Willander, M. Influence of the Polymer Concentration on the Electroluminescence of ZnO Nanorod/Polymer Hybrid Light Emitting Diodes. *J. Appl. Phys.* **2012**, *112*, 064324.

(14) Lupan, O.; Pauporte, T.; Viana, B. Low-Temperature Growth of ZnO Nanowire Arrays on p-Silicon (111) for Visible-Light-Emitting Diode Fabrication. *J. Phys. Chem. C* **2010**, *114*, 14781−14785.

(15) Son, D. I.; Kwon, B. W.; Park, D. H.; Seo, W.-S.; Yi, Y.; Angadi, B.; Lee, C.-L.; Choi, W. K. Emissive ZnO-Graphene Quantum Dots for White-Light-Emitting Diodes. *Nat. Nanotechnol.* **2012**, *7*, 465−471.

(16) Ling, B.; Sun, X. W.; Zhao, J. L.; Tan, S. T.; Dong, Z. L.; Yang, Y.; Yu, H. Y.; Qi, K. C. Electroluminescence From a n-ZnO Nanorod/p-$CuAlO_2$ Heterojunction Light-Emitting Diode. *Phys. E* **2009**, *41*, 635−639.

(17) Zhang, Q. B.; Guo, H. H.; Feng, Z. F.; Lin, L. L.; Zhou, J. Z.; Lin, Z. H. n-ZnO Nanorods/p-CuSCN Heterojunction Light-Emitting Diodes Fabricated by Electrochemical Method. *Electrochim. Acta* **2010**, *55*, 4889−4894.

(18) Xia, Y. N.; Yang, P. D.; Sun, Y. G.; Wu, Y. Y.; Mayers, B.; Gates, B.; Yin, Y. D.; Kim, F.; Yan, Y. Q. One-Dimensional Nanostructures: Synthesis, Characterization, and Applications. *Adv. Mater.* **2003**, *15*, 353−389.

(19) Kang, J.-W.; Choi, Y.-S.; Choe, M.; Kim, N.-Y.; Lee, T.; Kim, B.-J.; Tu, C. W.; Park, S.-J. Electrical and Structural Properties of Antimony-doped p-Type ZnO Nanorods with Self-corrugated Surfaces. *Nanotechnology* **2012**, *23*, 495712.

(20) Sun, X. W.; Ling, B.; Zhao, J. L.; Tan, S. T.; Yang, Y.; Shen, Y. Q.; Dong, Z. L.; Li, X. C. Ultraviolet Emission From a ZnO Rod Homojunction Light-Emitting Diode. *Appl. Phys. Lett.* **2009**, *95*, 133124.

(21) Chen, M.-T.; Lu, M.-P.; Wu, Y.-J.; Song, J.; Lee, C.-Y.; Lu, M.-Y.; Chang, Y.-C.; Chou, L.-J.; Wang, Z. L.; Chen, L.-J. Near UV LEDs Made with in Situ Doped p−n Homojunction ZnO Nanowire Arrays. *Nano Lett.* **2010**, *10*, 4387−4393.

(22) Li, P.-J.; Liao, Z.-M.; Zhang, X.-Z.; Zhang, X.-J.; Zhu, H.-C.; Gao, J.-Y.; Laurent, K.; Leprince-Wang, Y.; Wang, N.; Yu, D.-P. Electrical and Photoresponse Properties of an Intramolecular p−n Homojunction in Single Phosphorus-Doped ZnO Nanowires. *Nano Lett.* **2009**, *9*, 2513−2518.

(23) Nguyen, X. S.; Tay, C. B.; Fitzgerald, E. A.; Chua, S. J. ZnO Coaxial Nanorod Homojunction UV Light-Emitting Diodes Prepared by Aqueous Solution Method. *Small* **2012**, *8*, 1204−1208.

(24) Volnianska, O.; Boguslawski, P.; Kaczkowski, J.; Jakubas, P.; Jezierski, A.; Kaminska, E. Theory of Doping Properties of Ag Acceptors in ZnO. *Phys. Rev. B* **2009**, *80*, 245212.

(25) Li, Y.; Zhao, X.; Fan, W. Structural, Electronic, and Optical Properties of Ag-Doped ZnO Nanowires: First Principles Study. *J. Phys. Chem. C* **2011**, *115*, 3552−3557.

(26) Chai, G.; Lin, C.; Wang, J.; Zhang, M.; Wei, J.; Cheng, W. Density Functional Theory Simulations of Structures and Properties for Ag-Doped ZnO Nanotubes. *J. Phys. Chem. C* **2011**, *115*, 2907−2913.

(27) Thomas, M. A.; Sun, W. W.; Cui, J. B. Mechanism of Ag Doping in ZnO Nanowires by Electrodeposition: Experimental and Theoretical Insights. *J. Phys. Chem. C* **2012**, *116*, 6383−6391.

(28) Haynes, W. M. *CRC Handbook of Chemistry & Physics*, 91st ed.; Taylor and Francis Group: London, 2010.

(29) Han, X. G.; He, H. Z.; Kuang, Q.; Zhou, X.; Zhang, X. H.; Xu, T.; Xie, Z. X.; Zheng, L. S. Controlling Morphologies and Tuning the Related Properties of Nano/Microstructured ZnO Crystallites. *J. Phys. Chem. C* **2009**, *113*, 584−589.

(30) Na, S. H.; Park, C. H. First-Principles Study of the Surface Energy and the Atom Cohesion of Wurtzite ZnO and ZnS - Implications for Nanostructure Formation. *J. Kor. Phys. Soc.* **2010**, *56*, 498−502.

(31) Thi, M. P.; Hemery, H.; Durand, O.; Dammak, H. Orientation Distribution and Fiber Texture of Highly Oriented Piezoceramics: (1-

x)$PbMg_{1/3}Nb_{2/3}O_{3-x}PbTiO_3$ System. *Jpn. J. Appl. Phys.* **2004**, *43*, 8190−8194.
(32) Gong, Y.; Tu, R.; Goto, T. Microstructure and Preferred Orientation of Titanium Nitride Films Prepared by Laser CVD. *Mater. Trans.* **2009**, *50*, 2028−2034.
(33) Teke, A.; Ozgur, U.; Dogan, S.; Gu, X.; Morkoc, H.; Nemeth, B.; Nause, J.; Everitt, H. O. Excitonic Fine Structure and Recombination Dynamics in Single-crystalline ZnO. *Phys. Rev. B* **2004**, *70*, 195207.
(34) Meyer, B. K.; Alves, H.; Hofmann, D. M.; Kriegseis, W.; Forster, D.; Bertram, F.; Christen, J.; Hoffmann, A.; Strassburg, M.; Dworzak, M.; Haboeck, U.; Rodina, A. V. Bound Exciton and Donor-Acceptor Pair Recombinations in ZnO. *Phys. Status Solidi B* **2004**, *241*, 231−260.
(35) Zhu, L.; Li, J.; Ye, Z.; He, H.; Chen, X.; Zhao, B. Photoluminescence of Ga-doped ZnO Nanorods Prepared by Chemical Vapor Deposition. *Opt. Mater.* **2008**, *31*, 237−240.
(36) Xiu, F. X.; Yang, Z.; Mandalapu, L. J.; Zhao, D. T.; Liu, J. L. Photoluminescence Study of Sb-doped p-Type ZnO Films by Molecular-Beam Epitaxy. *Appl. Phys. Lett.* **2005**, *87*, 252102.
(37) Iwata, K.; Tampo, H.; Yamada, A.; Fons, P.; Matsubara, K.; Sakurai, K.; Ishizuka, S.; Niki, S. Growth of ZnO and Device Applications. *Appl. Surf. Sci.* **2005**, *244*, 504−510.
(38) Tampo, H.; Shibata, H.; Fons, P.; Yamada, A.; Matsubara, K.; Iwata, K.; Tamura, K.; Takasu, H.; Niki, S. The Effects of Thermal Treatments on the Electrical Properties of Phosphorus Doped ZnO Layers Grown by MBE. *J. Cryst. Growth* **2005**, *278*, 268−272.
(39) Wang, G.; Chu, S.; Zhan, N.; Zhou, H.; Liu, J. Synthesis and Characterization of Ag-doped p-Type ZnO Nanowires. *Appl. Phys. A* **2011**, *103*, 951−954.
(40) Thomas, M. A.; Cui, J. B. Investigations of Acceptor Related Photoluminescence from Electrodeposited Ag-doped ZnO. *J. Appl. Phys.* **2009**, *105*, 093533.
(41) Lu, J.; Liang, Q.; Zhang, Y.; Ye, Z.; Fujita, S. Improved p-Type Conductivity and Acceptor States in N-doped ZnO Thin Films. *J. Phys. D: Appl. Phys.* **2007**, *40*, 3177−3181.
(42) Haynes, J. R. Experimental Proof of the Existence of a New Electronic Complex in Silicon. *Phys. Rev. Lett.* **1960**, *4*, 361−363.
(43) Meyer, B. K.; Sann, J.; Lautenschlager, S.; Wagner, M. R.; Hoffmann, A. Ionized and Neutral Donor-Bound Excitons in ZnO. *Phys. Rev. B* **2007**, *76*, 184120.
(44) Kim, C. O.; Kim, S.; Shin, D. H.; Shin, D. Y.; Choi, S.-H.; Hwang, S. W.; Cha, N.-G.; Kang, S. Effect of Ga Doping Concentration on the Luminescence Efficiency of GaN Light-Emitting Diodes with Ga-doped ZnO Contacts. *Appl. Phys. B* **2012**, *109*, 283−287.
(45) Ahn, C. H.; Han, W. S.; Kong, B. H.; Cho, H. K. Ga-doped ZnO Nanorod Arrays Grown by Thermal Evaporation and Their Electrical Behavior. *Nanotechnology* **2009**, *20*, 015601.
(46) Werner, J. H.; Guttler, H. H. Barrier Inhomogeneities at Schottky Contacts. *J. Appl. Phys.* **1991**, *69*, 1522−1533.
(47) Norton, D. P.; Ivill, M.; Li, Y.; Kwon, Y. W.; Erie, J. M.; Kim, H. S.; Ip, K.; Pearton, S. J.; Heo, Y. W.; Kim, S.; Kang, B. S.; Ren, F.; Hebard, A. F.; Kelly, J. Charge Carrier and Spin Doping in ZnO Thin Films. *Thin Solid Films* **2006**, *496*, 160−168.
(48) Mangal, S.; Banerji, P. Studies on Metal/n-GaAs Schottky Barrier Diodes: The Effects of Temperature and Carrier Concentrations. *J. Appl. Phys.* **2009**, *105*, 083709.
(49) Cheung, S. K.; Cheung, N. W. Extraction of Schottky Diode Parameters From Forward Current-Voltage Characteristics. *Appl. Phys. Lett.* **1986**, *49*, 85−87.
(50) Yuksel, O. F.; Tugluoglu, N.; Gulveren, B.; Safak, H.; Kus, M. Electrical Properties of Au/Perylene-Monoimide/p-Si Schottky Diode. *J. Alloys Compd.* **2013**, *577*, 30−36.
(51) Demirezen, S.; Sonmez, Z.; Aydemir, U.; Altindal, S. Effect of Series Resistance and Interface States on the I-V, C-V and G/omega-V Characteristics in Au/Bi-doped Polyvinyl Alcohol (PVA)/n-Si Schottky Barrier Diodes at Room Temperature. *Curr. Appl. Phys.* **2012**, *12*, 266−272.
(52) Hu, J.; Pan, B. C. Electronic Structures of Defects in ZnO: Hybrid Density Functional Studies. *J. Chem. Phys.* **2008**, *129*, 154706.
(53) Gallino, F.; Pacchioni, G.; Di Valentin, C. Transition Levels of Defect Centers in ZnO by Hybrid Functionals and Localized Basis Set Approach. *J. Chem. Phys.* **2010**, *133*, 144512.
(54) Kumar, R.; Khare, N.; Bhalla, G. L.; Kamalasanan, M. N. Fabrication of ZnO/alpha-NPD:F-4-TCNQ Based Inorganic-Organic Hybrid Junction: Effect of Doping of Organic Layer on the Diode Like Characteristics. *Thin Solid Films* **2010**, *518*, E61−E64.
(55) Deng, R.; Yao, B.; Li, Y. F.; Yang, T.; Li, B. H.; Zhang, Z. Z.; Shan, C. X.; Zhang, J. Y.; Shen, D. Z. Influence of Oxygen/Argon Ratio on Structural, Electrical and Optical Properties of Ag-doped ZnO Thin Films. *J. Cryst. Growth* **2010**, *312*, 1813−1816.
(56) Lugo, F. J.; Kim, H. S.; Pearton, S. J.; Abernathy, C. R.; Gila, B. P.; Norton, D. P.; Wang, Y. L.; Ren, F. Rectifying ZnO:Ag/ZnO:Ga Thin-Film Junctions. *Electrochem. Solid State Lett.* **2009**, *12*, H188−H190.
(57) Song, Y.-W.; Kim, K.; Ahn, J. P.; Jang, G.-E.; Lee, S. Y. Physically Processed Ag-doped ZnO Nanowires for All-ZnO p−n Diodes. *Nanotechnology* **2009**, *20*, 275606.
(58) Lupan, O.; Pauporte, T.; Le Bahers, T.; Viana, B.; Ciofini, I. Wavelength-Emission Tuning of ZnO Nanowire-Based Light-Emitting Diodes by Cu Doping: Experimental and Computational Insights. *Adv. Funct. Mater.* **2011**, *21*, 3564−3572.